Dynamic recrystallization behaviour of spheroidal graphite iron. Application to cutting operations

Kevin Le Mercier, Michel Watremez, Eli Saúl Puchi-Cabrera, Laurent Dubar, Jean-Dominique Guerin, Laurence Fouilland Paille

Title: Dynamic recrystallization behaviour of spheroidal graphite iron. Application to cutting operations.

Author: K. Le Mercier M. Watremez E.S. Puchi-Cabrera L. Dubar J.D. Guérin L. Fouilland-Paillé

PII: S0924-0136(16)30312-0
DOI: http://dx.doi.org/doi:10.1016/j.jmatprotec.2016.08.036
Reference: PROTEC 14948

To appear in: *Journal of Materials Processing Technology*

Received date: 3-2-2016
Revised date: 29-8-2016
Accepted date: 30-8-2016

Please cite this article as: K. Le Mercier, M. Watremez, E.S. Puchi-Cabrera, L. Dubar, J.D. Guérin, L. Fouilland-Paillé, Dynamic recrystallization behaviour of spheroidal graphite iron. Application to cutting operations., *<![CDATA[Journal of Materials Processing Tech.]]>* (2016), http://dx.doi.org/10.1016/j.jmatprotec.2016.08.036

Dynamic recrystallization behaviour of spheroidal graphite iron. Application to cutting operations.

K. Le Mercier[a,c,*], M. Watremez[a,c], E.S. Puchi-Cabrera[a,c], L. Dubar[a,c], J.D. Guérin[a,c], L. Fouilland-Paillé[b,c]

[a] *UVHC, LAMIH UMR CNRS 8201, F-59313 Valenciennes, France*
[b] *Arts et Metiers ParisTech, MSMP EA7350, F-51006 Châlons en Champagne, France*
[c] *Institut Carnot Arts, F-75013 Paris, France*

Abstract

To increase the competitiveness of manufacturing processes, numerical approaches are unavoidable. Nevertheless, a precise knowledge of the thermo-mechanical behaviour of the materials is necessary to simulate accurately these processes. Previous experimental studies have provided a limited information concerning dynamic recrystallization of spheroidal graphite iron under hot cutting operations. The purpose of this paper is to develop a constitutive model able to describe accurately the occurrence of this phenomenon. Compression tests are carried out using a Gleeble 3500 thermo-mechanical simulator to determine the hot deformation behaviour of spheroidal graphite iron at high strains. Once the activation range of the dynamic recrystallization process is assessed, a constitutive model taking into account this phenomenon is developed and implemented in the Abaqus/Explicit software. Finally, a specific cutting test and its finite element model are introduced. The ability of the numerical model to predict the occurrence of dynamic recrystallization is then compared to experimental observations.

Keywords: SG iron, Hot cutting, Dynamic recrystallization, Finite element modelling.

*Corresponding author: Tel.: +33 3 27 51 14 54.
E-mail: kevin.lemercier@univ-valenciennes.fr (K. Le Mercier)

Nomenclature

Abbreviations

DIC	Digital image correlation
DRV	Dynamic recovery
DRX	Dynamic recrystallization
JMAK	Johnson-Mehl-Avrami-Kolmogorov model
SGI	Spheroidal graphite iron
STG	Sellars-Tegard-Garofalo model
WH	Work hardening

Arabic symbols

A	Material parameter
B_s, B_{ss}, B_y	Material parameters in the STG model, s^{-1}
D	Material parameter, s
m_s, m_{ss}, m_y	Material parameters in the STG model
n_{Av}	Avrami exponent
Q	Apparent activation energy for hot-working, $kJ.mol^{-1}$
q	Material parameter
Q_{DRX}	Apparent activation energy for dynamic recrystallization, $kJ.mol^{-1}$
R	Universal gas constant, $J.mol^{-1}.K^{-1}$
T	Absolute temperature, K
t	Time during which DRX occurs, s
$t_{0.5}$	Time for 50 percent recrystallization, s
X_v	Volume fraction recrystallized
Z	Zener-Hollomon parameter, s^{-1}

Greek symbols

δ_s, δ_{ss}, δ_y	Material parameters in the STG model, MPa
ε	Total effective strain

$\dot{\varepsilon}$	Effective strain rate, s^{-1}
ε_c	Critical strain for the onset of DRX
ε_r	Relaxation strain
θ_0	Work hardening rate of the material
$\mu(T)$	Temperature-dependent shear modulus, MPa
Σ	Flow stress defined in the user subroutine, MPa
σ	Flow stress after the onset of DRX, MPa
σ_c	Critical stress for the onset of DRX, MPa
σ_ε	Flow stress corresponding to the WH and DRV curve, MPa
σ_{eq}	Equivalent von Mises stress, MPa
σ_p	Peak stress, MPa
$\sigma_{sat}(T, \dot{\varepsilon})$	Hypothetical saturation stress, MPa
$\sigma_{ss}(T, \dot{\varepsilon})$	Steady-state flow stress, MPa
$\sigma_y(T, \dot{\varepsilon})$	Yield stress, MPa

1. Introduction

Over the past few years, austempered ductile iron emerged for its application in several fields such as automotive and railway industries. This specific spheroidal graphite iron provides an efficient compromise between specific mechanical strength, fracture toughness and resistance to abrasive wear. Therefore, this material is intended to substitute forged steels for the weight reduction of numerous manufactured components (Kovacs, 1987). To

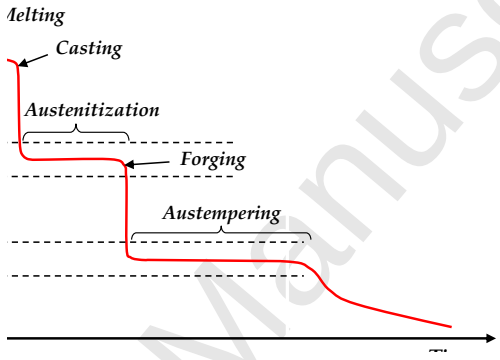

Figure 1: Heat treatment example for austempered ductile iron.

reach these enhanced mechanical properties, austempered ductile iron is obtained by a specific thermo-mechanical treatment (Figure 1). This consists in an austenitization of the cast iron in the temperature range 1123 - 1223 K followed by quenching to an austempering temperature of 523 to 623 K causing the transformation of the austenite phase into ausferrite. A combined casting and forging process prior to this specific quenching is often performed to reduce manufacturing costs (Meena and El Mansori, 2012). Also, with the aim of increasing the competitiveness, the removal of risers and feeder head is then performed at about 1273 K just after the casting operation. However, this stage can give rise to severe surface degradations under the cut surface, compromising the process viability.

A recent experimental investigation, performed by Fouilland and El Mansori (2013), allowed a better understanding of the mechanisms involved during the hot cutting of cast

specimens. During this operation, spheroidal graphite iron is stabilized in the austenite phase. The main softening process of austenite is dynamic recrystallization (DRX) due to its low stacking fault energy (Mirzadeh and Najafizadeh, 2010). Indeed, given the crystalline structure of austenite (fcc), cross-slip of dislocations is restricted and work hardening (WH) is only slightly moderated by dynamic recovery (DRV). The kinetic of DRV is too slow and the DRX process can then occur. The study of Fouilland and El Mansori (2013) revealed that the appearance of surface degradations is governed by a brittle-ductile transition, depending on the occurrence of DRX. When this softening process takes place a ductile behaviour leading to a precise cut is observed. Otherwise, a brittle behaviour arises promoting deep crack propagation under the cut surface.

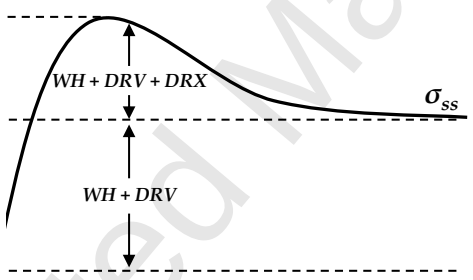

Figure 2: Typical dynamic recrystallization hardening curve.

The plastic flow stress evolution of a material which undergoes DRX is shown schematically in Figure 2. At stresses less than the critical stress for the onset of DRX (σ_c), the material undergoes both WH and DRV. However, once σ_c is exceeded DRX will become operative and the three processes will occur simultaneously. As the strain applied to the material increases, the volume fraction recrystallized dynamically (X_v) will also increase

and supersede the effect of WH and DRV. As a consequence, a work softening transient will occur, leading to the presence of a peak stress (σ_p) on the flow stress curve. As the strain applied to the material continuous to increase, the balance among WH, DRV and DRX will lead to the achievement of a steady-state stress (σ_{ss}), whose magnitude is equal to σ_c.

In numerical cutting models, the Johnson and Cook (1983) constitutive formulation is generally implemented because of its simplicity and numerical robustness (Limido et al., 2007). However, this empirical law describes the flow stress as a function of the total strain applied to the material, which is not a valid state parameter, by means of a simple parametric power-law relationship. Such a description would be incompatible with the evolution of flow stress mentioned above. Therefore, the present paper deals with the development of a specific constitutive model which not only allows the DRX process to be considered, but also that expresses the flow stress in terms of valid state parameters. Thus, the first challenge is to determine the activation range in which DRX occurs, by means of hot compression tests. Then, the selected model is implemented in the finite element analysis of a specific cutting operation. Finally, the prediction of the numerical model concerning the occurrence of DRX is discussed in relation to the experimental observations.

2. Experimental techniques

2.1. Material

The material employed for the present study is an ASTM A536 100-70-03 iron similar to that employed by Fouilland and El Mansori (2013). This spheroidal graphite iron (SGI) exhibits a pearlitic matrix at room temperature and a small amount of ferrite surrounding the graphite nodules, called bullseye ferrite (Figure 3). Its chemical composition is given in Table 1.

Figure 3: Optical micrograph of the ASTM A536 100-70-03 iron in its original state (etched with saturated nitric acid).

Element	C	Si	Mn	S	Cu	Ni	Cr	Mo	Mg
Composition (wt%)	3.35	2.72	0.16	0.009	0.87	0.71	<0.03	0.21	0.043

Table 1: Chemical composition of the ASTM A536 100-70-03 iron.

2.2. Mechanical characterization

The experiments were performed on a Gleeble 3500 thermo-mechanical testing machine. Compression specimens of 10 mm in diameter and 12 mm in length were tested under constant deformation conditions in a vacuum chamber. The samples were heated at 5 $K.s^{-1}$ to the testing temperature and then held for one minute at the test temperature. A K-thermocouple was welded at the half height of the specimen to ensure the temperature measurement. The tests were conducted at mean effective strain rates of 0.5, 1 and 5 s^{-1}, at nominal temperatures of 1073, 1173 and 1273 K. At the end of the tests, the specimens were air cooled. At least two tests were conducted for each deformation condition.

2.3. Cutting operation

These experiments were conducted on an orthogonal cutting test bench. The SGI specimens replicated the feeder head obtained just after casting. These were cylindrical

samples of 15 mm in height and 10 mm in diameter. Also, the fillet radius on the pin base was of 2.5 mm. At the beginning of the test, the specimens were heated in a furnace up to the required temperature. Then, they were clamped in a refractory insert bed, which prevented from heat losses. Finally, during the cutting operation, the high strength steel cutting tool moves against the cylinder, as shown in Figure 4. This experimental device includes a piezoelectric sensor for measuring cutting loads. A high speed camera records the cutting operation at a frequency of 15000 frames per second with a resolution of 768 x 648 pixels. A speckle pattern covering the tool allows the determination of the effective cutting velocity by means of a digital image correlation (DIC). The tests were performed three times at a temperature of 1273 K with a tool rake angle of -10 $^{\circ}$ and an initial cutting speed of 1.2 m.s^{-1}. The choice of the negative rake angle was based on the results of the study conducted by Fouilland and El Mansori (2013), which revealed that such rake angle allows the observation of the brittle-ductile transition.

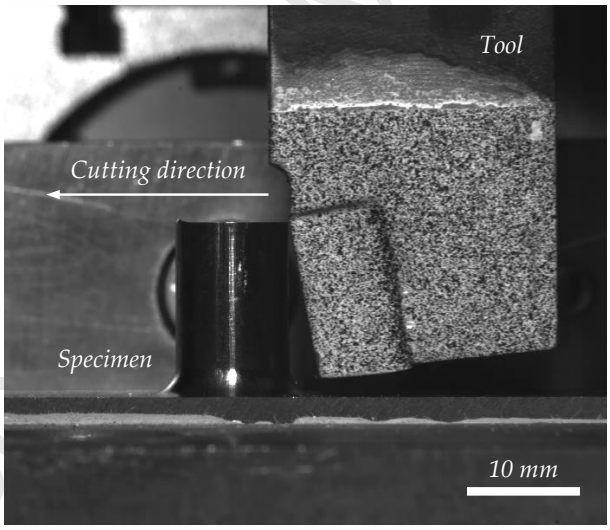

Figure 4: Clamped specimen and cutting tool.

3. Experimental results

3.1. Experimental results concerning the compression tests

Figure 5 illustrates the mean effective stress-effective strain curves obtained at different temperatures and strain rates. It was observed that the typical deviation of the flow stress values from the mean curve was about + or - 2 MPa. The experimental stress-strain curves exhibit the same shape as that portrayed in Figure 2, highlighting the occurrence of DRX during the compression tests.

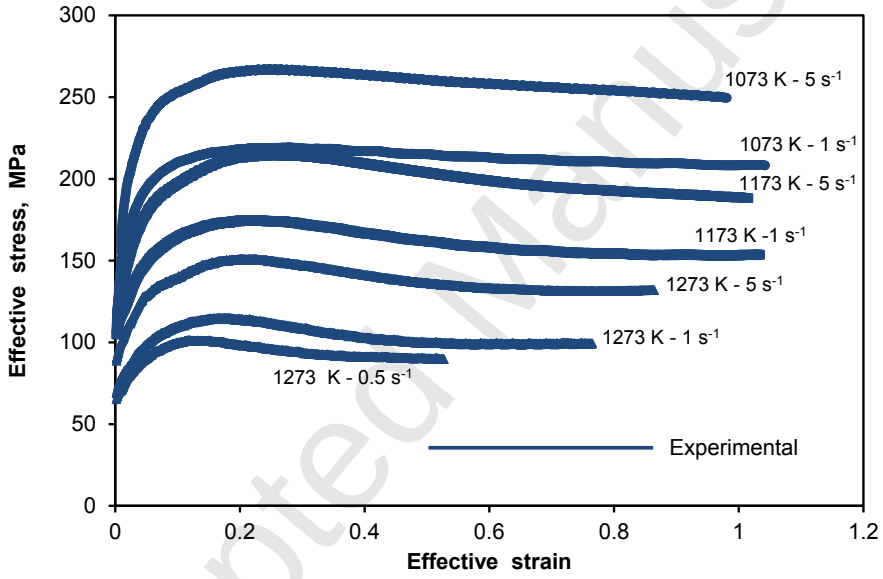

Figure 5: Effective-stress-effective strain curves obtained at different temperatures and strain rates.

The samples tested at 5 s^{-1} were observed using optical microscopy. Figures 6a and 6b show the optical micrographs of the samples deformed at 1073 K and 1173 K. These microstructures present a significant variation in their pearlitic matrix from the original state (Figure 3). Indeed, ferrite grains are more prominent and their size is finer. The microstructure of the sample deformed at 1273 K, exhibited in Figure 6c, has a pearlitic matrix and the crushed graphite nodules are surrounded by ferrite grains to a lesser extent.

The predominant change is observed with the pearlite grains, which have a finer size than in the original state.

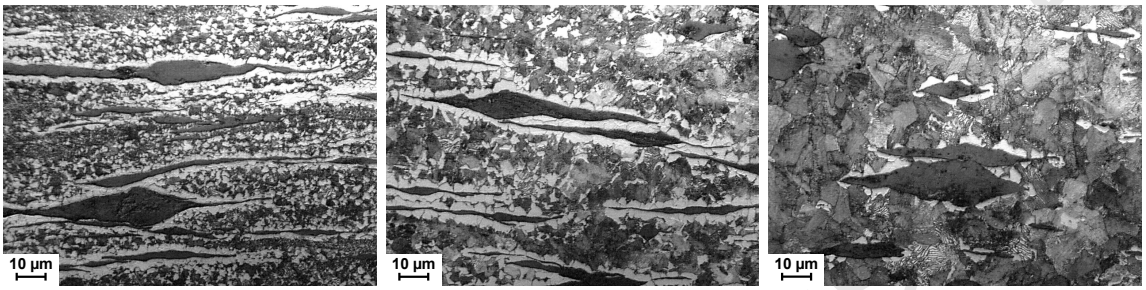

(a) 1073 K (b) 1173 K (c) 1273 K

Figure 6: Optical micrographs of the ASTM A536 100-70-03 iron deformed at 5 s^{-1} and different temperatures (etched with saturated nitric acid).

3.2. Experimental results concerning the cutting operation

Figure 7 clearly illustrates that the tool velocity obtained through DIC is not constant during the hot cutting operation. The first drop in cutting speed, observed at less than 1 ms, corresponds to the initial contact between the pin and the the tool. The second drop at approximately 3 ms, corresponds to the initiation of the shear band before the maximum force. Then, a constant cutting speed is achieved until the material failure leads to an increase in velocity due to an energy release. Finally, another decrease is observed, corresponding to the cutting of the residual material.

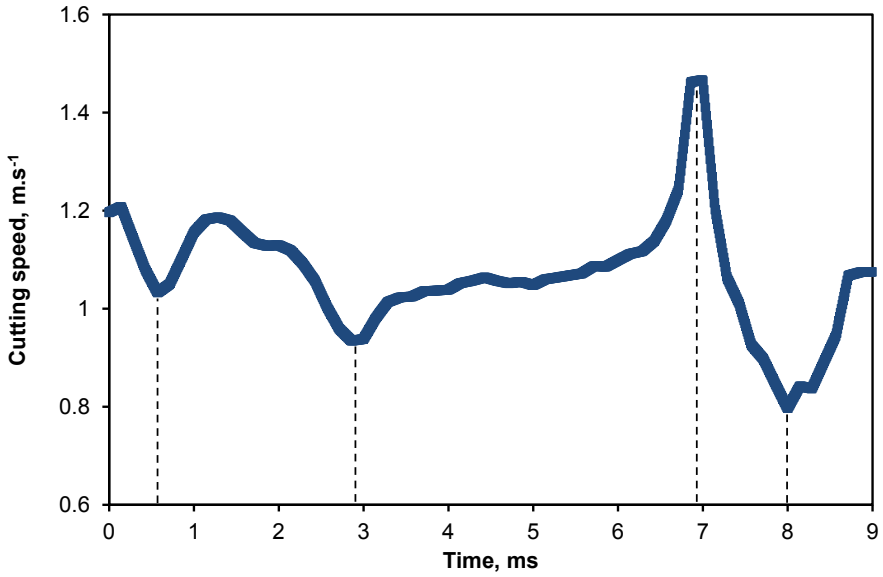

Figure 7: Effective tool velocity obtained through DIC.

Figure 8 shows the experimental cutting forces and also multiple pictures extracted from the recording of the cutting operation, whose main steps are described below.

1. The pin is in full contact with the tool and its base is deformed plastically,
2. A shear band is detected on the pin base, the cutting forces reach a maximum,

3. Crack initiation is observed on the pin base followed by a decrease of the cutting force,
4. The pin is completely removed, a small thickness of material is shaped by the tool, explaining the remaining forces.

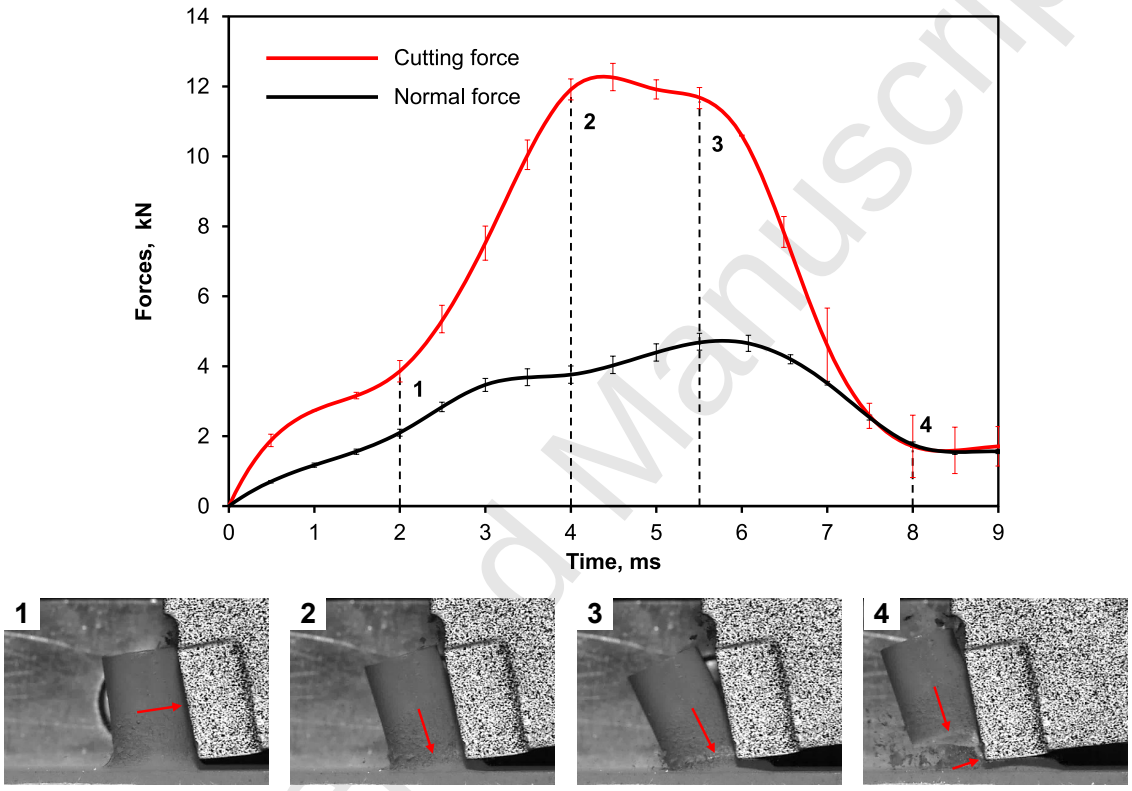

Figure 8: Axial and normal forces with the corresponding pictures recorded by the high speed camera.

In Figure 9, the observation in a cross section of the cut surface allows the understanding of the failure mechanism. The microstructure exhibits a large plastic deformation of the spheroidal graphite, which conforms with a ductile failure. Pearlite and ferrite grain sizes have decreased near the crushed spheroidal graphite, as in the metallographic observation of the compression test performed at 1273 K (Figure 6c).

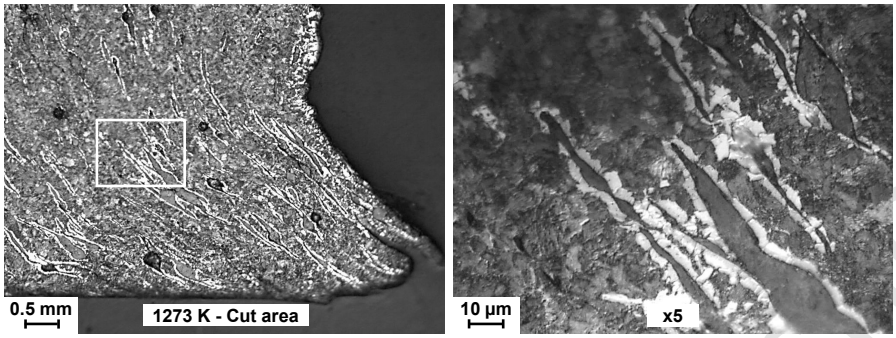

Figure 9: Optical micrograph of the specimen close to the cut surface (etched with saturated nitric acid).

4. Constitutive model employed for the description of the flow stress curves

In the past few years, several constitutive relations including DRX effects have been developed to describe the behaviour of austenite under hot working conditions. Most of these constitutive models are based on the dependence of different variables on the Zener-Hollomon parameter (Kim et al., 2003; Lin et al., 2008; Lurdos et al., 2008; Wang et al., 2012).

4.1. Description of the constitutive model

In the present work, the description of the flow stress curves corresponding to the SGI samples deformed under hot-working conditions has been carried out on the basis of the models earlier advanced by Puchi-Cabrera et al. for structural steels deformed under hot-working conditions [2011; 2013a; 2013b; 2014a; 2014b; 2015]. Accordingly, the flow stress data is employed for determining the main stress parameters characteristic of the deformation of the material under these conditions, which include: yield stress, critical stress for the onset of DRX, actual or hypothetical saturation stress (depending on deformation conditions) and actual steady-state stress. Additionally, both the Avrami exponent and the time required to achieve 50% DRX are determined from the work-softening transients present in some of the stress-strain curves. However, the model can be simplified on the ba-

sis of the experimental results reported by Jonas et al. (2009) and Quelennec et al. (2011), who demonstrated that, for a broad range of steel grades, the steady state stress is equal to the critical stress for the nucleation of DRX.

Thus, the work-hardening (WH) and dynamic recovery (DRV) transient of each stress-strain curve is described by means of the evolution equation derived from the work-hardening law advanced by Sah et al. (1969), which is expressed as:

$$\frac{d\sigma_\varepsilon}{d\varepsilon} = \frac{\mu(T)}{A}\left[1 - \left(\frac{\sigma_\varepsilon - \sigma_y\left(T,\dot{\varepsilon}\right)}{\sigma_{sat}\left(T,\dot{\varepsilon}\right) - \sigma_y\left(T,\dot{\varepsilon}\right)}\right)^2\right]\left[\frac{\sigma_{sat}\left(T,\dot{\varepsilon}\right) - \sigma_y\left(T,\dot{\varepsilon}\right)}{\sigma_\varepsilon - \sigma_y\left(T,\dot{\varepsilon}\right)}\right] \tag{1}$$

In the above evolution equation, σ_ε represents the current flow stress, σ_y the yield stress, σ_{sat} the hypothetical saturation stress, $\mu(T)$ the temperature-dependent shear modulus, $\dot{\varepsilon}$ the effective strain rate, T the deformation temperature and A a material parameter that could either be a constant or a function of deformation conditions through the Zener-Hollomon parameter, which is defined as $Z = \dot{\varepsilon}\exp\left(\frac{Q}{RT}\right)$ where Q is an apparent activation energy for hot deformation and R is the universal gas constant. As shown in the forthcoming, the constant A in the above equation is computed from the experimental stress-strain data corresponding to each stress-strain curve determined under constant deformation conditions.

Regarding the temperature-dependent shear modulus, it can be confidently computed from the equation (Kocks, 1976):

$$\mu(T) = 88884.6 - 37.3T, \text{ MPa} \tag{2}$$

The two stress parameters present in eq.(1) can also be expressed in terms of T and $\dot{\varepsilon}$ by means of the well established Sellars-Tegart-Garofalo (STG) model [1966]. For the

yield stress, its functional dependence on T and $\dot{\varepsilon}$ is expressed as:

$$\sigma_y\left(T,\dot{\varepsilon}\right)=\delta_y\sinh^{-1}\left(\left[\frac{\dot{\varepsilon}\exp\left(\frac{Q}{RT}\right)}{B_y}\right]^{1/m_y}\right) \tag{3}$$

Whereas, for the hypothetical saturation stress:

$$\sigma_{sat}\left(T,\dot{\varepsilon}\right)=\delta_s\sinh^{-1}\left(\left[\frac{\dot{\varepsilon}\exp\left(\frac{Q}{RT}\right)}{B_s}\right]^{1/m_s}\right) \tag{4}$$

In eqs. 3 and 4, δ_y, B_y and m_y, as well as δ_s, B_s and m_s represent material parameters and Q an apparent activation energy for hot deformation.

The actual steady-state stress (σ_{ss}), which as indicated above is considered to be equal to the critical stress for the onset of DRX (σ_c), can also be correlated with Z by means of the STG model, according to the following expression:

$$\sigma_{ss}\left(T,\dot{\varepsilon}\right)=\delta_{ss}\sinh^{-1}\left(\left[\frac{\dot{\varepsilon}\exp\left(\frac{Q}{RT}\right)}{B_{ss}}\right]^{1/m_{ss}}\right) \tag{5}$$

As in equation 4, δ_{ss}, B_{ss} and m_{ss} represent material parameters.

From the computational point of view, equation 1 is firstly integrated numerically. If the resulting value of σ_ε is less than σ_c ($\sigma_c=\sigma_{ss}$), the flow stress is determined by σ_ε ($\sigma=\sigma_\varepsilon$), otherwise, the flow stress should be computed from a second evolution equation, which includes the description of the work-softening transient associated to DRX. This second evolution law is expressed as:

$$\frac{d\sigma}{d\varepsilon}=\frac{\mu(T)}{A}\frac{1-\left[\frac{\sigma-\sigma_y+\Delta\sigma X_v}{\sigma_{sat}-\sigma_y}\right]^2}{\left[\frac{\sigma-\sigma_y+\Delta\sigma X_v}{\sigma_{sat}-\sigma_y}\right]}-\frac{n_{Av}\Delta\sigma(1-X_v)\ln 2}{\dot{\varepsilon}\;t_{0.5}^{n_{Av}}}\left[\frac{-t_{0.5}^{n_{Av}}\ln\left(1-X_v\right)}{\ln 2}\right]^{1-\frac{1}{n_{Av}}} \tag{6}$$

Thus, the incremental change in the flow stress with strain, once DRX becomes operative, is observed to depend on σ, σ_y, σ_{sat}, σ_{ss}, the dynamically recrystallized volume fraction, X_v, the Avrami exponent, n_{Av}, the time for 50% DRX, $t_{0.5}$, $\mu(T)$, $\dot{\varepsilon}$, T and constant A. Since plastic deformation of the material can occur under transient conditions involving arbitrary changes in temperature and strain rate, X_v should also be computed from the Johnson-Mehl-Avrami-Kolmogorov (JMAK) equation expressed in differential form:

$$\frac{dX_v}{dt} = \frac{n_{Av}(1-X_v)\ln 2}{t_{0.5}^{n_{Av}}}\left[\frac{-t_{0.5}^{n_{Av}}\ln\left(1-X_v\right)}{\ln 2}\right]^{1-\frac{1}{n_{Av}}} \tag{7}$$

However, in this case the change in the volume fraction recrystallized with time is also expressed in terms of the time required to achieved 50% DRX, $t_{0.5}$, which can be conveniently computed by means of the simple parametric relationship proposed by Jonas et al. (2009), expressed as:

$$t_{0.5} = D\left[\dot{\varepsilon}\exp\left(\frac{Q}{RT}\right)\right]^{-q}\exp\left(\frac{Q_{DRX}}{RT}\right)\ , \text{s} \tag{8}$$

In the above equation, D represents a material constant weakly dependent on the austenitic grain size, whereas q and Q_{DRX} represent a material parameter and the apparent activation energy for dynamic recrystallization, respectively. Thus, the constitutive description of the material is represented by equations 1 through 8. Clearly, two important features can be observed. Firstly, the flow stress is absolutely independent of the total strain (ε) applied to the material. Secondly, that given the determination of the flow stress from the numerical integration of two evolution laws, such a parameter can be readily evaluated when the deformation of the material occurs under transient deformation conditions, which are characteristic of actual industrial hot deformation processes. The experimental flow stress data determined at different deformation temperatures and strain rates constitutes the raw data for the rational computation of the different material parameters involved in these relationships.

4.2. Identification of the different parameters involved in the constitutive model

The precise determination of the different stress parameters involved in the constitutive description of material, as well as the time required to achieve 50% DRX, can be conducted by means of the individual modelling of each stress-strain curve determined under constant conditions of temperature and strain rate. Figures 10 through 12 illustrate the comparison of the experimental stress-strain curves and the predicted ones employing equations (1) and (6) of the constitutive formulation presented in the previous section. The accurate description of the experimental curves suggests that their individual modelling allows a precise and reliable identification of all the parameters of interest indicated above. Table 2 summarizes the value of the relevant parameters that were determined for each deformation condition.

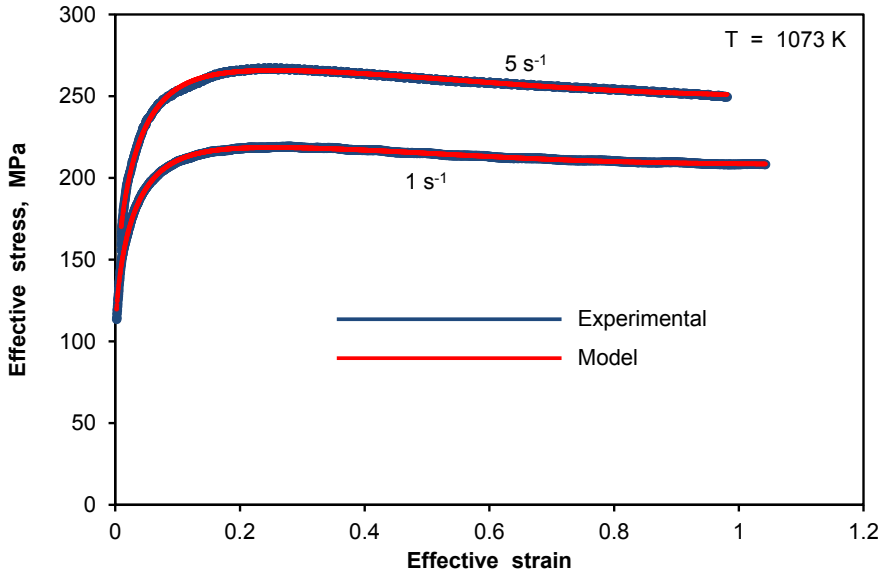

Figure 10: Comparison of the experimental stress-strain curves and the constitutive formulation at 1073 K.

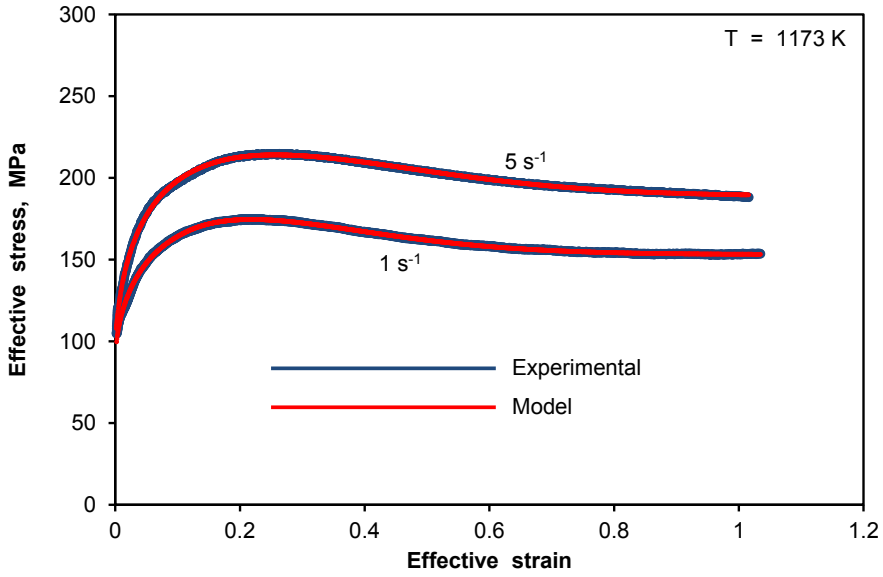

Figure 11: Comparison of the experimental stress-strain curves and the constitutive formulation at 1173 K.

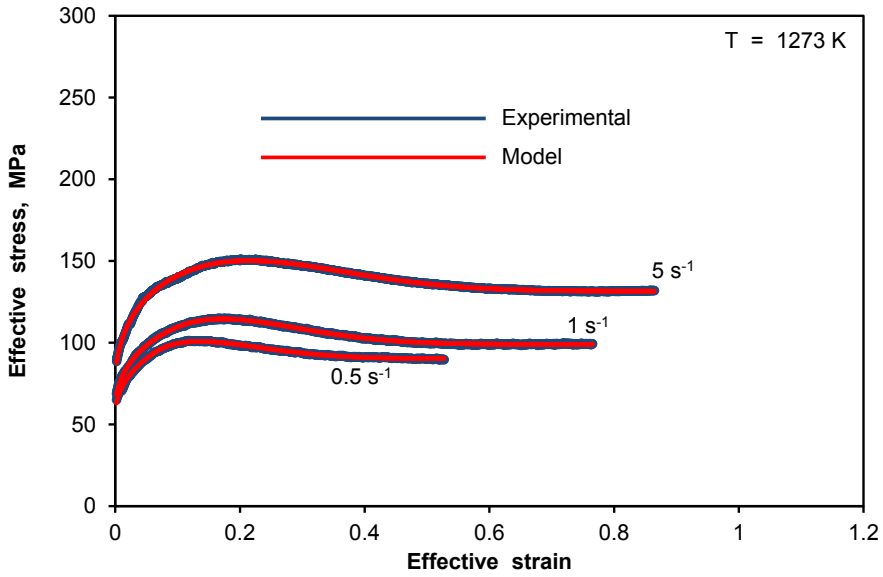

Figure 12: Comparison of the experimental stress-strain curves and the constitutive formulation at 1273 K.

σ_y, MPa	σ_{peak}, MPa	σ_{sat}, MPa	σ_{ss}, MPa	$t_{0.5}$, s	A, MPa	$\dot{\varepsilon}$, s^{-1}	T, K
55.1	101.3	125.9	91.6	0.31	207.6	0.5	1273
59.5	114.9	127.5	99.0	0.19	155.3	1	1273
75.4	151.0	157.9	131.4	0.05	100.9	5	1273
84.2	174.9	182.1	153.1	0.28	84.0	1	1173
87.1	214.7	218.7	188.9	0.07	54.9	5	1173
92.2	219.3	219.3	208.2	0.41	37.8	1	1073
102.3	267.2	267.2	249.3	0.09	30.8	5	1073

Table 2: Relevant parameters involved in the description of the individual stress-stain curves.

However, in order to formulate a global constitutive equation able to predict the flow stress of the material under arbitrary deformation conditions, the functional dependence of σ_y, σ_{sat}, σ_{ss}, $t_{0.5}$ and A (if any) on $\dot{\varepsilon}$, T should also be accurately established.

Previous studies conducted on 20MnCr5 steel deformed under hot-working conditions (Puchi-Cabrera et al., 2014a) indicated that a single activation energy value of approximately 283.3 kJ.mol^{-1} could be satisfactorily employed for the computation of the Zener-Hollomon parameter (Z), as well as for the corresponding description of σ_y, σ_{sat}, σ_{ss} and $t_{0.5}$ as a function of deformation temperature and strain rate. Therefore, in the present work the same value will be employed for both purposes. Thus, Figure 13 illustrates the change in σ_y, σ_{sat} and σ_{ss} as a function of Z, as well as their corresponding description according to the STG model (eqs. 3 through 5). Table 3 summarizes the value of the different material parameters involved.

δ_y, MPa	B_y, s^{-1}	m_y	δ_s, MPa	B_s, s^{-1}	m_s	δ_{ss}, MPa	B_{ss}, s^{-1}	m_{ss}
19.0	1.77E+08	3	104.2	3.47E+10	4.96	88.3	1.13E+11	3.74

Table 3: Materials parameters involved in description of σ_y, σ_{sat} and σ_{ss} as a function of Z, according to the STG model.

As can be observed from Figure 13, the predicted change in each parameter with Z, indicated by the solid lines, describes quite satisfactorily the experimental data, which provides a reliable formulation for modelling purposes. An interesting feature that can be observed from this figure is that related to the behaviour exhibited by σ_{sat} and σ_{ss}. The curve corresponding to the change in σ_{sat} with Z, in the temperature and strain rate intervals explored in the present work, is always above that corresponding to the change in σ_{ss}. However, as Z increases above a value of approximately 10^{16} s^{-1}, both curves tend to approach each other, which suggests that DRX will occur to a lesser extent and therefore, that DRV will be the only operative dynamic restoration process.

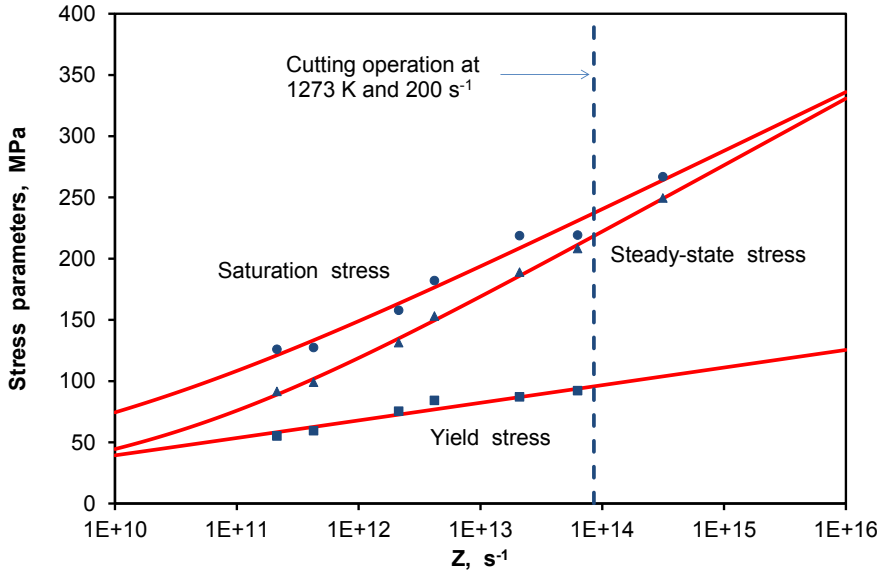

Figure 13: σ_y, σ_{sat} and σ_{ss} as a function of Z.

The Z value corresponding to the deformation conditions involved in the cutting operation for the removal of risers and feeder head after casting are also shown on the plot. As indicated above, this operation is conducted at a temperature of 1273 K and a strain rate of approximately 200 s^{-1}. Figure 13 clearly shows that under these deformation conditions DRX is still operative, contributing to the ductile behaviour of the material during the

cutting operation. However, it also shows that as the temperature decreases and the strain rate increases, the extent to which DRX continues to occur is more limited.

Regarding the temperature and strain rate description of $t_{0.5}$, Figure 14 clearly illustrates that the simple parametric relationship given in eq.(8) constitutes a quite satisfactory approach for the computation of such a parameter under arbitrary deformation conditions.

Figure 14: Evolution of the time required to achieve 50% DRX as function of Z.

As indicated on the plot, this relationship can be simplified further by assuming that the apparent activation energy for DRX has the same magnitude than that for hot deformation, which reduces the number of material parameters in the global constitutive formulation without compromising the accuracy of the model prediction. The values of the different constants involved in eq.(8) are shown on the plot.

Another important consideration of the proposed constitutive formulation involves the temperature and strain rate dependence of constant A, as can be clearly observed from

Table 2. Previous work conducted both on C-Mn, 20MnCr5 and Fe-Mn23-C0.6 steels [Puchi-Cabrera et al., 2011; 2013a; 2013b; 2014a; 2014b; 2015] indicates that this constant in general does not exhibit any significant dependence on T and $\dot{\varepsilon}$. However, in the present case it can be clearly observed that such a constant exhibits a significant dependence on deformation conditions, which should be taken into consideration into the global constitutive formulation. Thus, Figure 15 highlights the change in A as a function of Z, which clearly indicates that an increase in Zener-Hollomon parameter value leads to a significant and unexpected increase in the athermal work-hardening rate of the material, $\theta_0 = \mu/A$.

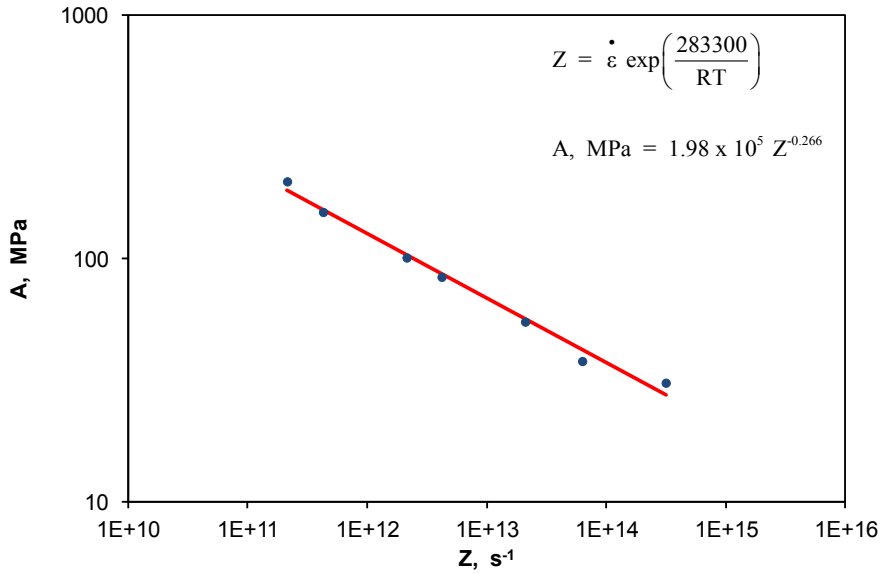

Figure 15: A as a function of Z.

The final step in the determination of the constitutive formulation of the material under investigation involves a global optimization of the experimental data in order to adjust further the constants indicated in Figure 15, related to the parameter A, as well as the determination of a unique value for the Avrami exponent, n_{Av}, which characterizes the DRX kinetics. Figures 16 through 18 show the comparison between predicted and experimental stress-strain curves at different temperatures and strain rates. These plots clearly illustrate

that the proposed constitutive description for the SGI under consideration allows a satisfactory prediction of the flow stress, as well as of the work-hardening and work-softening transients present on the stress-strain curves. Therefore, the formulation represents a reliable tool for the computation of the flow stress required in finite element codes employed for the numerical simulation of the cutting operations indicated above, regardless if these processes occur either under constant or transient deformation conditions.

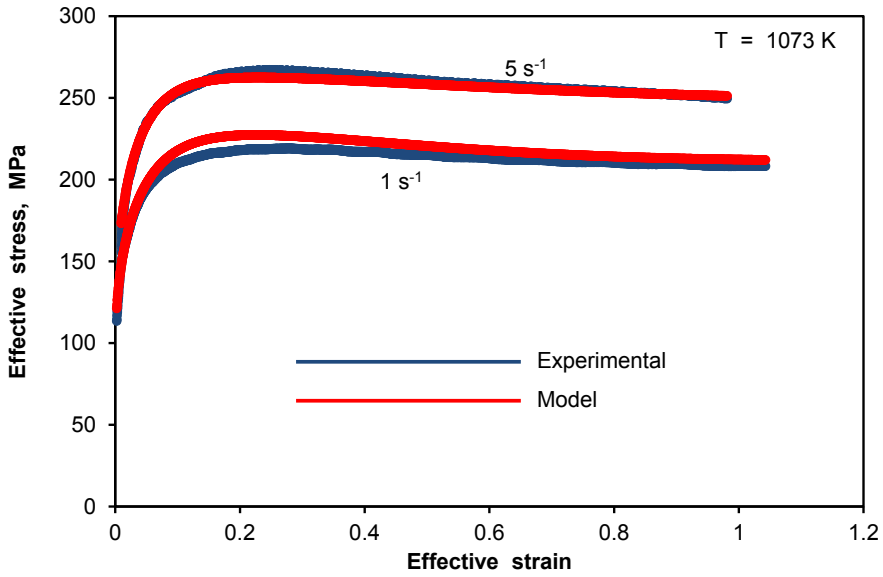

Figure 16: Comparison between predicted and experimental stress-strain curves at 1073 K.

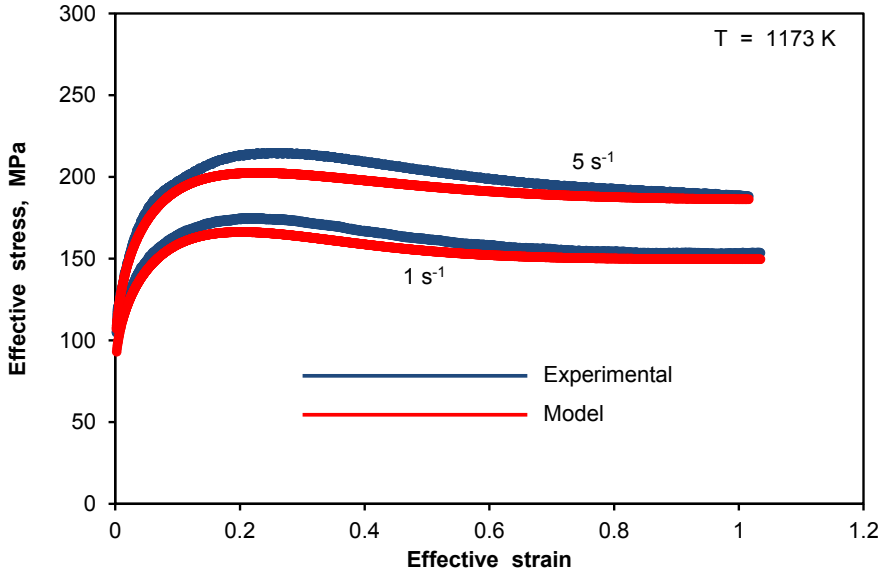

Figure 17: Comparison between predicted and experimental stress-strain curves at 1173 K.

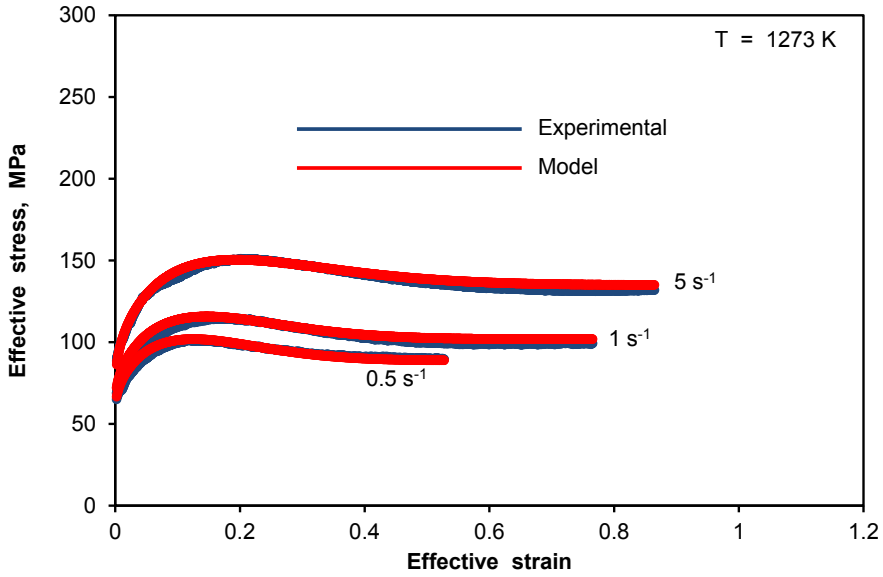

Figure 18: Comparison between predicted and experimental stress-strain curves at 1273 K.

Finally, Figure 19 exhibits a comparison between the experimental and computed values of the flow stress, which allows a further evaluation of the accuracy of the constitutive formulation regarding the computation of such a parameter. As can be clearly observed, the maximum relative error between the computed and predicted values of the flow stress is in the range of 8%. The plot includes the final expression for the computation of constant A, as well as the Avrami exponent that can be confidently employed for the description of the DRX kinetics.

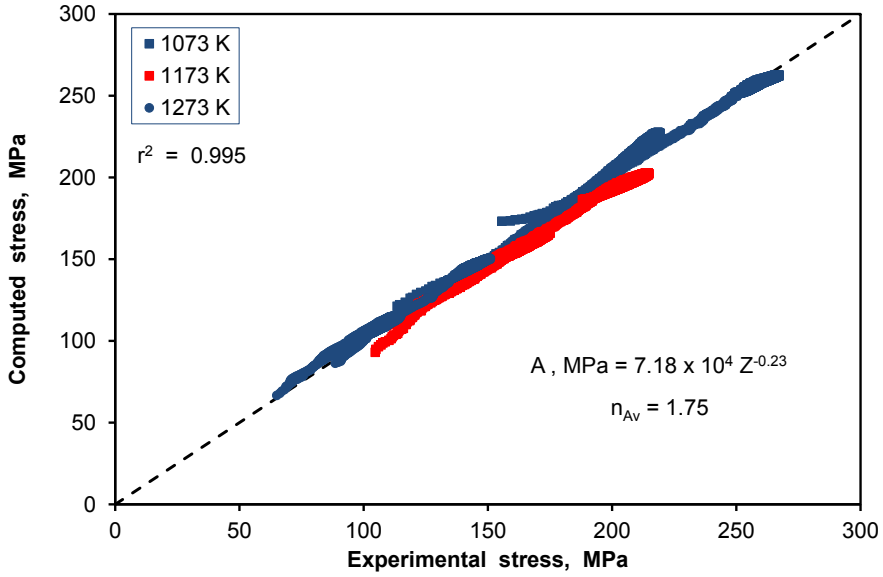

Figure 19: Maximum relative error between the computed and predicted values of the flow stress.

5. Finite element modelling of the cutting operation

5.1. Finite element model description

Finite element modelling and analysis of the cutting operation were performed with the Abaqus/Explicit software. Figure 20 shows the initial mesh of the workpiece and the cutting tool. The specimen was meshed using 8-nodes 3D solid elements (C3D8RT). A higher mesh density was applied to the pin, as compared to the rest of the model.

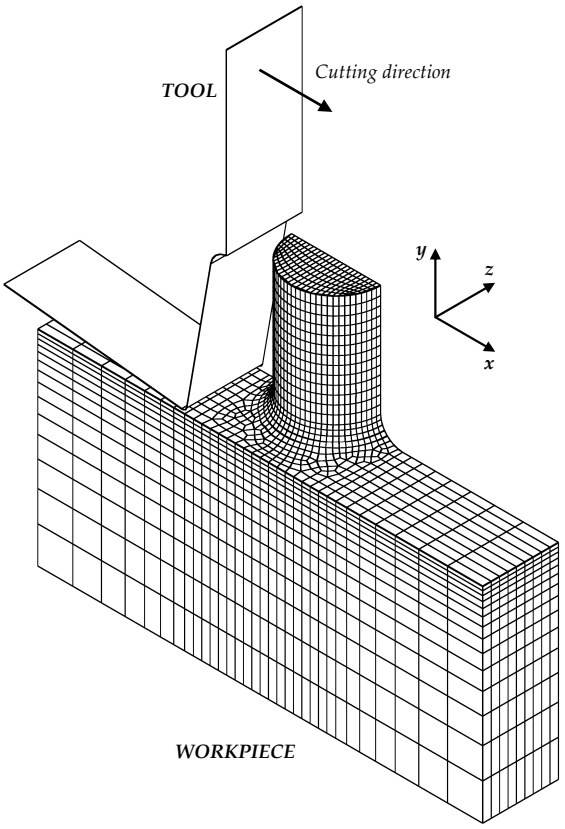

Figure 20: Isometric view of the initial mesh configuration.

In order to reduce the computing time of this analysis, only half of both the specimen and the tool were modelled. This results in 9710 elements. A symmetry condition on the z-axis was applied to both right faces of the workpiece and the tool. Appropriate boundary conditions were applied to constrain the bottom, front and left faces of the specimen. The tool, which is considered as a rigid surface, was constrained to move in the cutting direction, at a speed, which varies with time, as shown in Figure 7. No other displacements were allowed. The contact between the tool and the workpiece was modelled using a Coulomb's friction law. The friction coefficient has been identified by an inverse method and set to an almost constant value of 0.2. The workpiece was modelled as an elastic-plastic material

with isotropic hardening.

5.2. Implementation of the constitutive model

Since the cutting operation is assumed to be performed at a mean constant temperature and strain rate, the integrated version of the constitutive formulation presented in section 4 was implemented using a VUHARD user subroutine (Figure 21).

$$\varepsilon_r = \frac{1}{2}\frac{A}{\mu(T)}(\sigma_{sat}(T,\dot{\varepsilon}) - \sigma_y(T,\dot{\varepsilon}))$$

$$\varepsilon_c = -\varepsilon_r \ln\left[1 - \left(\frac{\sigma_{ss}(T,\dot{\varepsilon}) - \sigma_y(T,\dot{\varepsilon})}{\sigma_{sat}(T,\dot{\varepsilon}) - \sigma_y(T,\dot{\varepsilon})}\right)^2\right]$$

If $\varepsilon < \varepsilon_c$

$$\sigma_\varepsilon = \sigma_y(T,\dot{\varepsilon}) + (\sigma_{sat}(T,\dot{\varepsilon}) - \sigma_y(T,\dot{\varepsilon}))\left[1 - \exp\left(-\frac{\varepsilon}{\varepsilon_r}\right)\right]^{1/2}$$

Required variables

$$\Sigma = \sigma_\varepsilon$$

$$\left[\frac{\partial\Sigma}{\partial\varepsilon}\right]_{(T,\dot{\varepsilon})}, \left[\frac{\partial\Sigma}{\partial\dot{\varepsilon}}\right]_{(T,\varepsilon)}, \left[\frac{\partial\Sigma}{\partial T}\right]_{(\varepsilon,\dot{\varepsilon})}$$

Else

$$t = \frac{\varepsilon - \varepsilon_c}{\dot{\varepsilon}}$$

$$X_v = 1 - \exp\left[-\ln(2)\left(\frac{t}{t_{0.5}}\right)^{n_{Av}}\right]$$

$$\Delta\sigma = X_v(\sigma_{sat}(T,\dot{\varepsilon}) - \sigma_{ss}(T,\dot{\varepsilon}))$$

Required variables

$$\Sigma = \sigma_\varepsilon - \Delta\sigma$$

$$\left[\frac{\partial\Sigma}{\partial\varepsilon}\right]_{(T,\dot{\varepsilon})}, \left[\frac{\partial\Sigma}{\partial\dot{\varepsilon}}\right]_{(T,\varepsilon)}, \left[\frac{\partial\Sigma}{\partial T}\right]_{(\varepsilon,\dot{\varepsilon})}$$

Figure 21: Algorithm defined in the VUHARD subroutine.

The variables to be defined in the subroutine are the flow stress, Σ, and its variations with respect to the total effective strain, the effective strain rate and the temperature.

The volume fraction recrystallized, X_v, was set as a solution-dependent variable within the subroutine. The critical strain for the onset of DRX (ε_c), the relaxation strain (ε_r) and the time during which DRX occurs (t) were introduced.

As mentioned in the previous section, the cutting operation is conducted at a mean temperature of 1273 K and a mean strain rate of approximately 200 s^{-1}. Furthermore, the high cutting speed allows no time for heat transfer between the tool and the workpiece material. Thus, the model was assumed to be adiabatic. According to Soo et al. (2004), this assumption is generally used for the simulation of high-speed manufacturing processes. The initial temperature of the test was applied to the specimen. No fracture criterion is introduced in this simulation as the emphasis is put on the beginning of the hot cutting operation corresponding to the first 4 ms. Since the constitutive law has been implemented in its integrated form, it assumes that during the cutting operation the mean strain rate remains constant and therefore, no effect of crack propagation has been taken into consideration concerning the evolution of the volume fraction recrystallized dynamically. In order to take into account changes in temperature and strain rate during the cutting operation, the constitutive law should be implemented in its differential formulation.

5.3. Simulation results

Figure 22 illustrates the comparison between the predicted forces before the crack initiation and the experimental forces. The normal force is predicted quite satisfactorily,

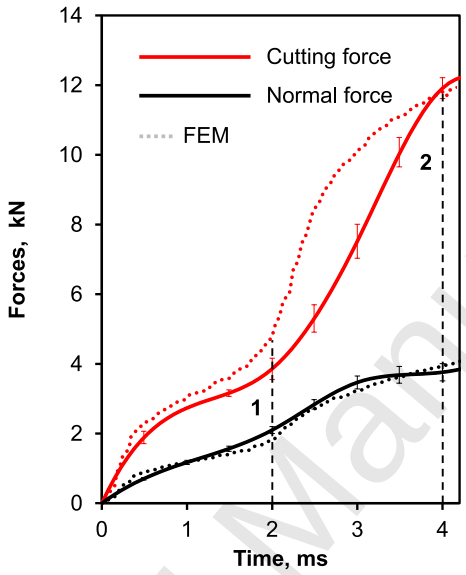

Figure 22: Comparison between experimental and predicted forces.

whereas the cutting force is clearly overestimated between the steps 1 and 2. However at 4 ms, the prediction errors are respectively about 2.8 percent and 1.8 percent for the cutting and normal forces. The gap between the finite element model and the experimental results can be explained by the fact that the SGI specimen is not perfectly clamped in its insert. The relative velocity between the tool and the pin is then less than expected at the beginning of the test. This, results in a time lag between the predicted cutting force and the actual one.

Figure 23 shows the von Mises stress (σ_{eq}) distribution within the specimen during the cutting operation. The fillet radius on the pin base is an area of stress concentration. The average value of von Mises stresses in the fillet radius at 4 ms is about 250 MPa. Under these deformation conditions, DRX is then operative as the effective stress associated to the WH and DRV curve is greater than the critical stress for the onset of DRX.

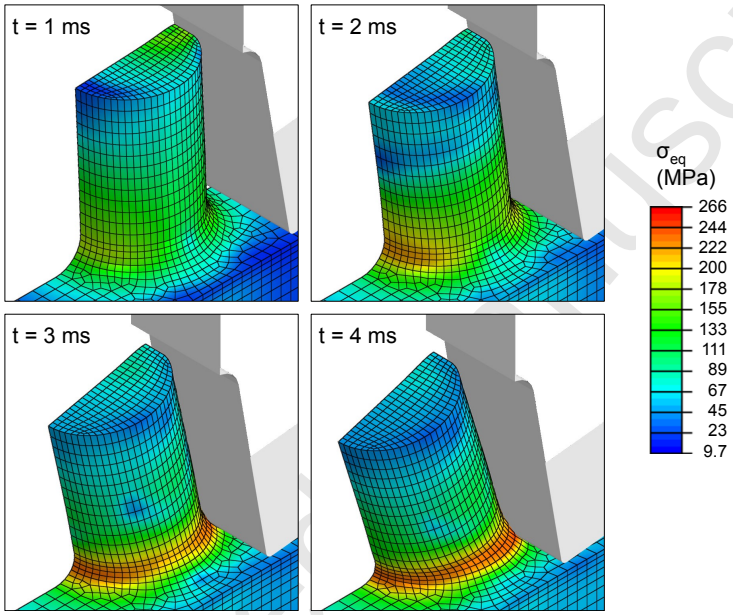

Figure 23: Stress distribution (von Mises) within the specimen during the cutting operation.

The constitutive model allows the prediction of DRX within the specimen during the cutting operation. Figure 24 shows the change of X_v as a function of time. The finite element analysis shows that DRX occurs at the top of the specimen due to the compression loading at the beginning of the cutting operation. Indeed, the average value of stresses in the top of the pin at 1 ms is about 170 MPa. Furthermore, the strain rate decreases in the top of the pin as the tool moves forward. DRX is then operative at the top of the pin as the effective stress associated to the WH and DRV curve is still greater than the critical stress for the onset of DRX.

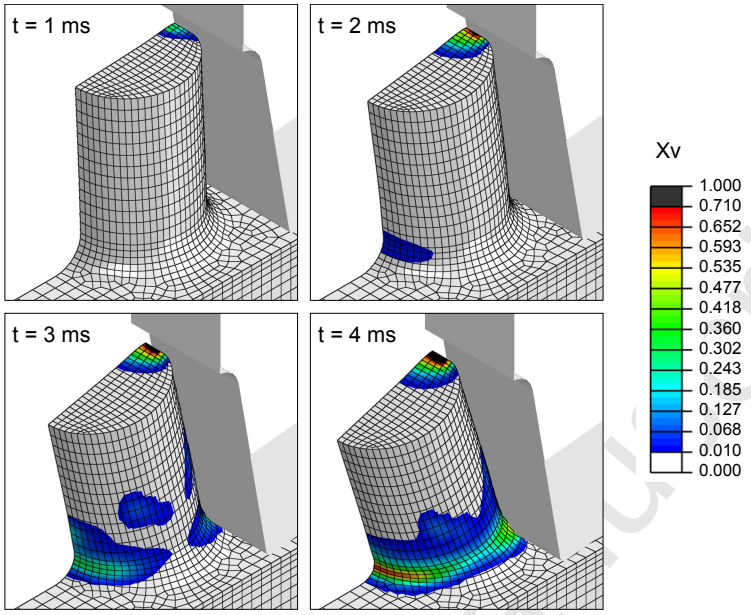

Figure 24: Predicted dynamically recrystallized volume fraction, X_v, within the specimen during the cutting operation.

DRX is initiated within the shear band when the pin is in full contact with the tool, at 2 ms. The value of X_v is then about 1 percent. As the tool moves forwards, X_v increases within the shear band and reaches approximately 70 percent. Finally, the finite element model predicts the occurrence of DRX within the shear zone, which agrees with the experimental observations.

6. Conclusions

A methodology aimed at studying the influence of dynamic recrystallization during the hot cutting of an ASTM A536 100-70-03 has been proposed. A specific constitutive model considering dynamic recrystallization effects on the material hot deformation behaviour, has been developed. The thermo-mechanical response of the ASTM A536 100-70-03 iron has been investigated by means of compression tests on a Gleeble device. The occurrence

of dynamic recrystallization has been determined. A typical cutting process has been modelled both from the experimental and numerical point of view. The numerical predictions agree with the experimental results and highlighted some explanations concerning the occurrence of dynamic recrystallization within the shear zone. Currently, further investigations are being carried out in order to validate the proposed constitutive description, by modelling other cutting configurations. Also, a fracture criterion is being characterized for the spheroidal graphite iron, in order to investigate the competition between the material fracture and the occurrence of DRX during the cutting operation.

7. Acknowledgements

The present research work has been supported by the ARTS Carnot Institute and was made possible through the collaboration between MSMP and LAMIH laboratories. The authors gratefully acknowledge the support of this institute. They also express their sincere thanks to R. Moulart (Associate Professor at MSMP Research Group), T. Garçon (Assistant Engineer at LAMIH laboratory), B. Laurent (Manufacturing workshop manager at LAMIH laboratory) and J. Voisin (Assistant Engineer at MSMP Research Group) for their valuable support. Professor Puchi-Cabrera gratefully acknowledges the financial support of the program Campus France.

References

Fouilland, L., El Mansori, M., 2013. Experimental study of the brittle ductile transition in hot cutting of SG iron specimens. Journal of Materials Processing Technology 213, 201 – 213.

Johnson, G. R., Cook, W. H., 1983. A constitutive model and data for metals subjected to large strains, high strain rates and high temperatures. Proceedings of Seventh International Symposium on Ballistics 21, 541 – 547.

Jonas, J. J., Quelennec, X., J., L., Martin, E., 2009. The Avrami kinetics of dynamic recrystallization. Acta Materialia 57 (9), 2748 – 2756.

Kim, S. I., Lee, Y., Byon, S. M., 2003. Study on constitutive relation of AISI 4140 steel subject to large strain at elevated temperatures. Journal of Materials Processing Technology 140, 84 – 89, proceedings of the 6th Asia Pacific Conference on materials Processing.

Kocks, U. F., 1976. Laws for work-hardening and low-temperature creep. Journal of Engineering Materials and Technology 98, 76–85.

Kovacs, B. V., 1987. Development of austempered ductile iron (ADI) for automobile crankshafts. Journal of Heat Treating 5, 55 – 60.

Limido, J., Espinosa, C., Salan, M., Lacome, J. L., 2007. SPH method applied to high speed cutting modelling. International Journal of Mechanical Sciences 49, 898 – 908.

Lin, Y. C., Chen, M. S., Zhong, J., 2008. Constitutive modeling for elevated temperature flow behavior of 42CrMo steel. Computational Materials Science 42, 470 – 477.

Lurdos, O., Montheillet, F., Damamme, G., 2008. Empirical and physically based flow rules relevant to high speed processing of 304L steel. International Journal of Material Forming 1, 1431 – 1434.

Meena, A., El Mansori, M., 2012. Drilling performance of green austempered ductile iron (ADI) grade produced by novel manufacturing technology. The International Journal of Advanced Manufacturing Technology 59, 9 – 19.

Mirzadeh, H., Najafizadeh, A., 2010. Prediction of the critical conditions for initiation of dynamic recrystallization. Materials and Design 31, 1174 – 1179.

Puchi-Cabrera, E. S., Guérin, J. D., Barbier, D., Dubar, M., Lesage, J., 2013a. Plastic deformation of structural steels under hot-working conditions. Materials Science and Engineering: A 559, 268 – 275.

Puchi-Cabrera, E. S., Guérin, J. D., Dubar, M., Staia, M. H., Lesage, J., Chicot, D., 2014a. Constitutive description for the design of hot-working operations of a 20MnCr5 steel grade. Materials & Design 62, 255 – 264.

Puchi-Cabrera, E. S., Guérin, J. D., Dubar, M., Staia, M. H., Lesage, J., Chicot, D., 2015. Constitutive description of FeMn23C0.6 steel deformed under hot-working conditions. International Journal of Mechanical Sciences 99, 143 – 153.

Puchi-Cabrera, E. S., Staia, M. H., 2011. Constitutive description of a low C-Mn steel deformed under hot-working conditions. Materials Science and Engineering: A 528 (6), 2843 – 2858.

Puchi-Cabrera, E. S., Staia, M. H., Guérin, J. D., Lesage, J., Dubar, M., Chicot, D., 2013b. Analysis of the work-hardening behavior of CMn steels deformed under hot-working conditions. International Journal of Plasticity 51, 145 – 160.

Puchi-Cabrera, E. S., Staia, M. H., Guérin, J. D., Lesage, J., Dubar, M., Chicot, D., 2014b. An experimental analysis and modeling of the work-softening transient due to dynamic recrystallization. International Journal of Plasticity 54, 113 – 131.

Quelennec, X., Bozzolo, N., Jonas, J. J., Loge, R., 2011. A New Approach to Modeling the Flow Curve of Hot Deformed Austenite. ISIJ International 51 (6), 945–950.

Sah, J. P., Richardson, G., Sellars, C. M., 1969. Recrystallization during hot deformation of nickel. Journal of the Australian Institute of Metals 14, 292–297.

Sellars, C. M., McTegart, W. J., 1966. On the mechanism of hot deformation. Acta Metallurgica 14, 1136–1138.

Soo, S. L., Aspinwall, D. K., Dewes, R. C., 2004. 3D FE modelling of the cutting of Inconel 718. Journal of Materials Processing Technology 150, 116 – 123.

Wang, J., Xiao, H., Xie, H., Xu, X., Gao, Y., 2012. Study on hot deformation behavior of carbon structural steel with flow stress. Materials Science and Engineering: A 539, 294 – 300.